





**Behavior of chiral bands in  $^{128,130}\text{Cs}$  and  $^{130}\text{La}$** Pooja Siwach  and P. Arumugam \**Department of Physics, Indian Institute of Technology Roorkee, Roorkee-247667, Uttarakhand, India*L. S. Ferreira  and E. Maglione *Centro de Física e Engenharia de Materiais Avançados CeFEMA, Instituto Superior Técnico, Universidade de Lisboa, Avenida Rovisco Pais, P1049-001 Lisboa, Portugal*

(Received 1 December 2020; accepted 2 February 2021; published 26 February 2021)

The nonadiabatic quasiparticle approach is applied to study chiral doublet bands in  $^{128}\text{Cs}$ ,  $^{130}\text{Cs}$ , and  $^{130}\text{La}$ . The calculated energy spectra and electromagnetic transition probabilities reproduce quite well the experimental data.  $^{130}\text{Cs}$  turns out to be a better example for chiral symmetry breaking than  $^{128}\text{Cs}$ , unlike it has been suggested in earlier studies. We present the first theoretical investigation of chiral geometry and its correlation with the single-particle configurations in  $^{130}\text{La}$  to understand the mode of chirality, i.e., static or vibrational.

DOI: [10.1103/PhysRevC.103.024327](https://doi.org/10.1103/PhysRevC.103.024327)**I. INTRODUCTION**

Intensive experimental and theoretical efforts have substantially improved our understanding of chiral symmetry breaking in atomic nuclei [1] in the last two decades. Only triaxial nuclei can exhibit this phenomenon, and hence it is a direct evidence of the breaking of axial symmetry in atomic nuclei. Chiral symmetry breaking through chiral doublet bands has been observed in odd-odd, odd- $A$ , and even-even nuclei [2–6], specifically in mass regions  $A \approx 80, 100, 130$ , and 190 [2].

Chiral symmetry breaking in atomic nuclei is manifested through the degeneracy of energy levels. Electromagnetic (EM) decay properties are also crucial signatures of chirality, which can be measured. These measurements of transition probabilities have been beneficial in identifying chiral doublet bands [7–9].

Aplanar orientation of the resultant of proton, neutron, and core angular momenta is one of the most undoubted properties of chiral bands. The  $g$  factor's measurement can help to reveal the underlying geometry formed by these three angular momenta. A recent study [10] in this direction suggested the planar orientation at the band head of the yrast band in  $^{128}\text{Cs}$ . However, due to experimental limitations, the measurements of the  $g$  factors for the higher levels having smaller half-lives is not possible at the moment. On the theoretical front, chiral geometry can be interpreted unambiguously through the projection of angular momentum on the three intrinsic axes ( $K$  plots) [11,12], and the probability distribution on the tilted planes (azimuthal plots) [12–14]. These investigations have been done in many studies [12,14,15] to illustrate chiral geometry.

Among the reported odd-odd nuclei in the  $A \approx 130$  region exhibiting chirality, we find that  $^{128,130}\text{Cs}$  and  $^{130}\text{La}$  are of special interest.  $^{128}\text{Cs}$  was proposed to be the best known

example of chirality [7], whereas, in  $^{130}\text{Cs}$ , the neutron Fermi level lies in the relatively higher orbital of the  $h_{11/2}$  subshell as compared to  $^{128}\text{Cs}$ , indicating a better condition for chirality. Furthermore, in  $^{130}\text{La}$  (isotone of  $^{128}\text{Cs}$ ) the EM transition probabilities were measured recently [8] and signatures of static chirality were not observed.

Here we apply the nonadiabatic quasiparticle approach [16,17] to study chiral doublet bands in  $^{128}\text{Cs}$ ,  $^{130}\text{Cs}$ , and  $^{130}\text{La}$ . In this approach, the rotation-particle coupling is carried out in such a way that the matrix elements of the even-even core appear explicitly. This treatment provides the opportunity to utilize the experimental energies of the core, which in turn reduces the dependence on the moment of inertia. Chiral geometry can be studied conveniently in this approach [17]. Chiral geometry has been investigated in  $^{128}\text{Cs}$  [12] and  $^{130}\text{Cs}$  [14] within the angular momentum projection (AMP) approach without and with configuration mixing, respectively. However, such a detailed theoretical study is required for chiral doublet bands in  $^{130}\text{La}$ . Therefore, we present here the first theoretical investigation of chiral bands in  $^{130}\text{La}$  through chiral geometry and its correlation with single-particle configurations.

Since the nature of chirality is sensitive to the occupation probability of valence quasiparticle levels and the coupling of the valence proton and neutron to the core, a detailed analysis of the contribution of single-particle levels is required. We investigate chiral bands in all three nuclei at the same footing by considering the proper single-particle configuration mixing unlike Ref. [12]. We aim to explore chirality behavior in these nuclei and compare the results based on the variations in angular momenta orientations and single-particle configurations with angular momentum.

**II. THEORETICAL FRAMEWORK**

We treat the triaxial odd-odd system by coupling the valence proton and neutron to the even-even core. The total

\*Corresponding author: arumugam@ph.iitr.ac.in

Hamiltonian for such a system is given by

$$H = H_{\text{intr}}^{p(n)} + H_{\text{core}} + V_{\text{np}}. \quad (1)$$

Here,  $H_{\text{intr}}^{p(n)}$  describes the single-particle (proton and neutron) motion in the intrinsic frame, which can be further expanded as follows:

$$H_{\text{intr}}^{p(n)} = H_{\text{sp}}^{p(n)} + H_{\text{pair}}^{p(n)}, \quad (2)$$

where  $H_{\text{sp}}^{p(n)}$  comprises a Woods-Saxon potential [18] as the nuclear mean field along with the spin-orbit and Coulomb potentials.  $H_{\text{pair}}^{p(n)}$  accounts for the residual pairing interaction treated within the BCS approach.  $H_{\text{core}}$  is the Hamiltonian of the triaxial core and  $V_{\text{np}}$  is the residual interaction between the valence neutron and proton. Since in the nuclei studied here, the residual  $np$  interaction is found to be not important, we avoid the corresponding formalism. However, the details in this regard can be found in Ref. [16].

By coupling the core, proton, and neutron wave functions in the way given in Ref. [16], the matrix element for the total Hamiltonian given in Eq. (1) can be written as

$$\begin{aligned} & \langle q'_p q'_n K', IM | H | q_p q_n K, IM \rangle \\ &= (\mathcal{E}_{q_p} + \mathcal{E}_{q_n}) \delta_{KK'} \delta_{q_p q'_p} \delta_{q_n q'_n} \\ &+ \sum_{j_p j_n \Omega'_p \Omega'_n \Omega'_z} \sum_{j=|j_p-j_n|}^{j_p+j_n} \mathbb{W}_{KK'}^{j_p j_n j \Omega'_p \Omega'_n \Omega'_z} \\ &\times f_{u_n v_n} f_{u_p v_p} \mathcal{F}^p \mathcal{F}^n \\ &+ \delta_{KK'} f_{u_n v_n} f_{u_p v_p} \langle \psi_{p'} \psi_{n'} | V_{np} | \psi_p \psi_n \rangle, \end{aligned} \quad (3)$$

where  $q_i$  ( $i = p$  or  $n$ , for proton or neutron) represents the quasiparticle states, and  $\mathcal{E}_{q_i}$  are the quasiparticle energies. The quantity  $j_i$  represents the single-particle angular momentum and  $\Omega_i$  its projection on the 3 axis.  $I$  is the total angular momentum and its projections on the 3 axis and  $z$  axis are denoted by  $K$  and  $M$ , respectively. The quantity  $\mathcal{F}^i$  represents the integrated radial components of the single-particle wave functions (with  $r$  in the denominator), i.e.,  $\int dr \phi_{j_i \Omega_i}^*(r) \phi_{j_i \Omega_i}(r)$  involving the mixing coefficients implicitly. The function  $\psi_i$  in the matrix element of  $V_{np}$  denotes the single-particle wave function. The factor  $f_{u_i v_i}$  is given by

$$f_{u_i v_i} = u_i u_{i'} + v_i v_{i'}. \quad (4)$$

Here the square of  $u$  and  $v$  provides the probability of a single-particle level to be unoccupied and occupied, respectively. The quantity  $\mathbb{W}_{K'K}^{j_p j_n j \Omega'_p \Omega'_n \Omega'_z}$  is given by

$$\begin{aligned} & \mathbb{W}_{K'K}^{j_p j_n j \Omega'_p \Omega'_n \Omega'_z} \\ &= \langle j_p j_n j \Omega'_p \Omega'_n, IMK' | H_{\text{core}} | j_p j_n j \Omega_p \Omega_n, IMK \rangle \\ &= \sum_{RK_R K'_R} A_{j_p j_n j \Omega'_p \Omega'_n, RK'_R}^{IK'} A_{j_p j_n j \Omega_p \Omega_n, RK_R}^{IK} \\ &\times \sum_{\rho} C_{K'_R}^{R\rho} E_{TR\rho} C_{K_R}^{R\rho}. \end{aligned}$$

Here  $A$ 's are the amplitudes comprising the Clebsch-Gordan coefficients which appear through the angular momentum

couplings, and the normalization constant [16].  $R$  and  $K_R$  are the angular momentum of the core and its projection on the 3 axis, respectively. The quantities  $E_{TR\rho}$  and  $C_{K_R}^{R\rho}$  represent the core energies and wave functions for its level  $\rho$ .

The total wave function for an odd-odd system is given by

$$\begin{aligned} \Psi_{IM} = & \sqrt{\frac{2I+1}{16\pi^2}} \sum_{\Omega_p \Omega_n \Omega_K} a_{\Omega_p \Omega_n \Omega_K}^I [D_{MK}^I | j_p \Omega_p \rangle | j_n \Omega_n \rangle \\ & + (-1)^{I-j_p-j_n} D_{M-K}^I | j_p - \Omega_p \rangle | j_n - \Omega_n \rangle], \end{aligned} \quad (5)$$

where  $a$ 's are the mixing coefficients which are further utilized in calculating the reduced EM transition probabilities [17]. The orientation of the total angular momentum ( $I$ ) in the intrinsic frame can be obtained from its profile  $\mathcal{P}^I(\theta, \phi)$  [15,17] on the  $(\theta, \phi)$  plane.  $\theta$  and  $\phi$  are the tilted angles [12] of the total angular momentum with respect to the intrinsic frame.  $\theta$  is the angle between 3 axis and  $I$ , and  $\phi$  the angle between the projection of  $I$  on the 1-2 plane and 1 axis. The profile  $\mathcal{P}^I(\theta, \phi)$  can be found by taking the direction of  $I$  along the  $z$  axis in the laboratory frame. The expression for  $\mathcal{P}^I(\theta, \phi)$  is given by [15,17]

$$\begin{aligned} \mathcal{P}^I(\theta, \phi) = & \int_0^{2\pi} d\alpha' \sum_{v'} \left| \sum_{Kv} a_{vK}^I \sqrt{\frac{2I+1}{16\pi^2}} \right. \\ & \times [D_{IK}^I(\alpha', \theta, \pi - \phi) \delta_{v',v} \\ & \left. + (-1)^{I-K} D_{I,-K}^I(\alpha', \theta, \pi - \phi) \delta_{v',-v} \right]^2, \end{aligned} \quad (6)$$

where  $v$  represents the configuration of the single-particle wave functions.

### III. RESULTS AND DISCUSSION

We investigate the positive parity chiral doublet bands B1 (yrast) and B2 (side) in  $^{128,130}\text{Cs}$  and  $^{130}\text{La}$  which are identified [7,19–21] to be built on the  $[\pi h_{11/2} \otimes \nu h_{11/2}]$  configuration. With the detailed analysis of calculated quantities, like rotational energies and EM transition probabilities, we consider the deformation parameters ( $\beta_2, \beta_4, \gamma$ ) to be (0.21,  $-0.008$ ,  $28^\circ$ ), (0.2,  $-0.001$ ,  $28^\circ$ ), and (0.229,  $-0.004$ ,  $23^\circ$ ) for  $^{128}\text{Cs}$ ,  $^{130}\text{Cs}$ , and  $^{130}\text{La}$ , respectively. These values are within the range suggested for the ground state in the macroscopic-microscopic studies [22], and those considered in Refs. [8,12,14]. The off-diagonal matrix elements of the total Hamiltonian are attenuated by a factor  $\rho = 0.9, 0.8$ , and  $0.9$ , in  $^{128}\text{Cs}$ ,  $^{130}\text{Cs}$ , and  $^{130}\text{La}$ , respectively. A stronger attenuation in the case of  $^{130}\text{Cs}$  signifies the overestimation in the strength of the Coriolis interaction due to the neutron Fermi level lying in higher orbitals of  $h_{11/2}$  compared to  $^{128}\text{Cs}$  and  $^{130}\text{La}$ . The  $^{126}\text{Xe}$ ,  $^{128}\text{Xe}$ , and  $^{128}\text{Ba}$  are considered as the cores in case of  $^{128}\text{Cs}$ ,  $^{130}\text{Cs}$ , and  $^{130}\text{La}$ , respectively. We used method 2 of Ref. [23] to calculate the core wave functions with the parameters  $\{C(\text{MeV}^3), I_0(\text{MeV}^{-1})\}$  obtained as  $\{0.012, 10.3\}$ ,  $\{0.006, 6.7\}$ , and  $\{0.022, 14.3\}$  for  $^{126}\text{Xe}$ ,  $^{128}\text{Xe}$ , and  $^{128}\text{Ba}$ , respectively.

Through the experimental studies of  $^{128,130}\text{Cs}$  and  $^{130}\text{La}$ , major features of chirality are established. For example,

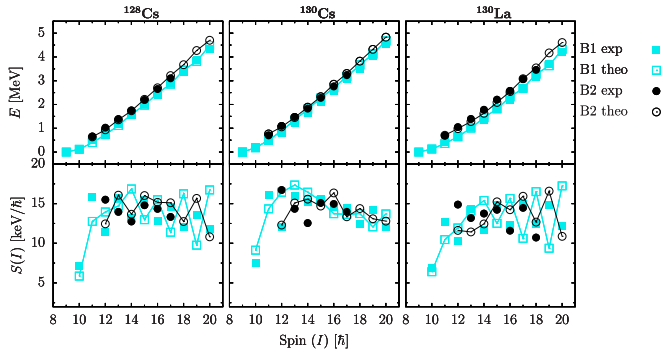


FIG. 1. Rotational energies (top panels) and odd-even staggering (bottom panels) for bands B1 (yrast) and B2 (side) in  $^{128}\text{Cs}$ ,  $^{130}\text{Cs}$ , and  $^{130}\text{La}$ . The experimental data are taken from Refs. [7,8,19].

chiral symmetry breaking in the intrinsic frame is restored in the laboratory frame, which in turn leads to the observation of degenerate  $\Delta I = 1$  same parity bands. Furthermore, due to the alignment of proton and neutron angular momenta perpendicular to that of the core, the Coriolis interaction is not strong. Hence, the odd-even staggering in energies given by the parameter  $S(I) = [E(I) - E(I - 1)]/2I$  has a smooth dependence on spin in chiral doublet bands. The calculated rotational energies given in Fig. 1 are in a very nice agreement

with the measured data for all three nuclei. The odd-even staggering in energies has a comparable magnitude with the measured ones, while the phase in the case of band B1 is opposite at higher spins. This behavior originates from the contributions of single-particle configurations, and is explained later.

Another interesting feature of chirality can be observed through EM transition probabilities. Distinguished by the handedness only, chiral partners should have comparable intraband EM transition probabilities. Furthermore, the selection rules [24] suggest the odd-even staggering in  $B(M1)$  values and  $B(M1)/B(E2)$  ratios. However, these rules are derived within the particle rotor model for a special case of single-particle configurations at  $\gamma = 30^\circ$ , and hence can vary slightly with the  $\gamma$  or the model used. The measurements of these probabilities have contributed a lot in identifying the degenerate bands as chiral partners. For instance, on the one hand, these measurements in  $^{128}\text{Cs}$  [7] claimed it to be the best example of having chirality. On the other hand, the measurement of these probabilities in  $^{132}\text{La}$  [7] discarded it to be a chiral nucleus due to the large difference in intraband  $B(E2)$  values. We analyze such important reduced EM probabilities for the intraband and interband transitions corresponding to the bands B1 and B2 in  $^{128,130}\text{Cs}$  and  $^{130}\text{La}$  nuclei. The factors  $g_p$  and  $g_n$  are attenuated by a factor of 0.7 in calculations

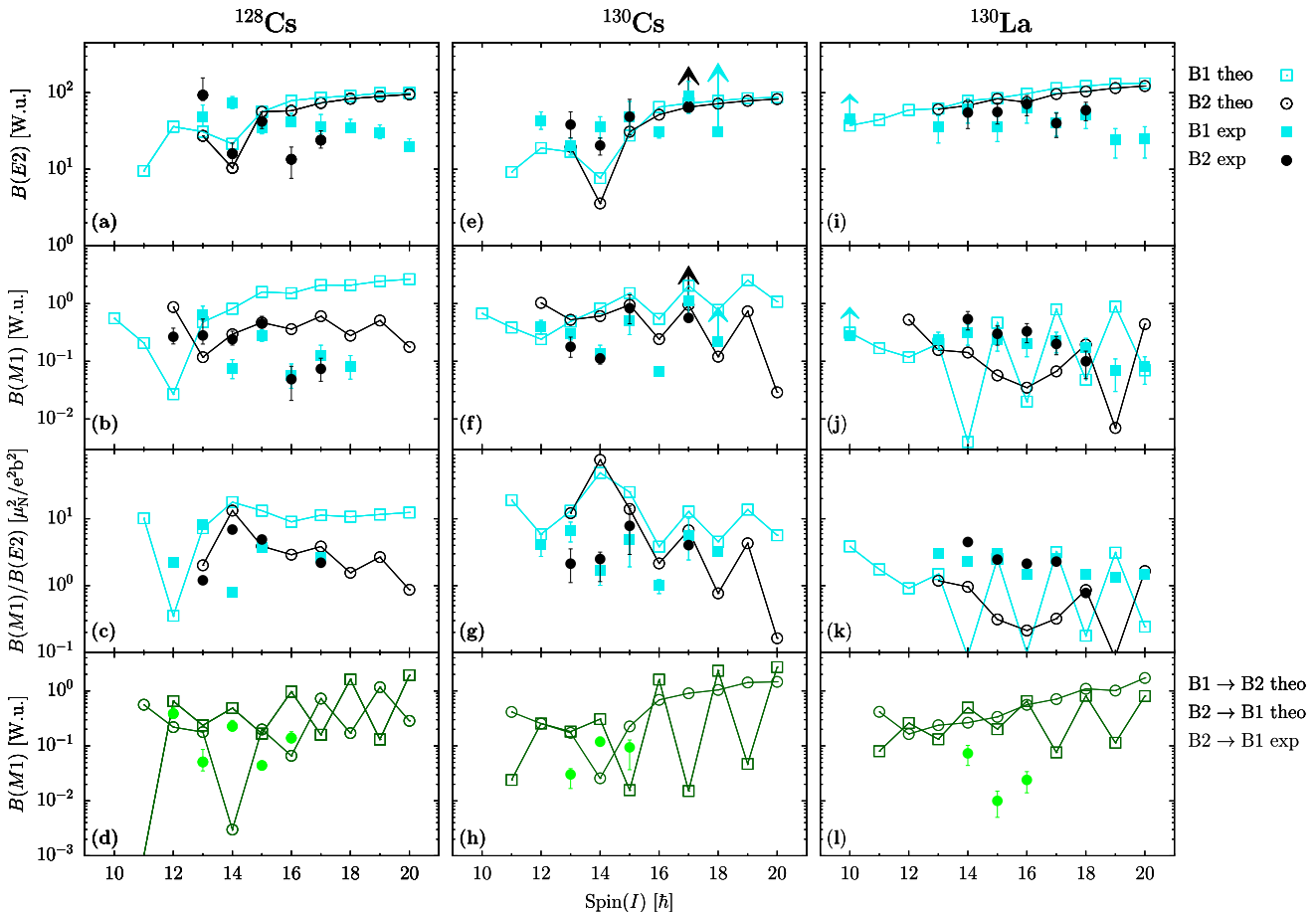


FIG. 2. Reduced EM transition probabilities, i.e., intraband [(a), (e), (i)]  $B(E2)$ , [(b), (f), (j)]  $B(M1)$ , and [(c), (g), (k)]  $B(M1)/B(E2)$ , and interband [(d), (h), (l)]  $B(M1)$  of the doublet bands B1 and B2 in  $^{128}\text{Cs}$ ,  $^{130}\text{Cs}$ , and  $^{130}\text{La}$ . The experimental data are taken from Refs. [2,7,8].

of all three nuclei such that  $g_{p,n} = 0.7g_{p,n}^{(\text{free})}$  as suggested in Ref. [25]. Following the same reference, we neglect the proton and neutron terms for calculating  $B(E2)$  since their contribution is much smaller as compared to that of the core. The results compared with the measured ones are given in Fig. 2.

In the case of  $^{128}\text{Cs}$ , the  $B(E2)$  values for both bands are identical and agree well with the experimental data in the lower spin region, whereas they deviate at higher spins. This deviation can be attributed to the limitations of the frozen nuclear shape assumption. An abrupt behavior at  $I = 14\hbar$  in band B1 appears to be due to the change in single-particle configurations. The intraband  $B(M1)$  values and  $B(M1)/B(E2)$  ratios are comparable with the experimental data. The staggering in these values is larger in the case of band B2 as compared to band B1 (very weak). The extent of these agreements is comparable with other theoretical calculations based on the AMP approach [12]. The interband  $B(M1)$  values for transitions from band B2 to B1 agree in magnitude with the measured ones, but are opposite in phase. Also, the interband  $B(M1)$  values for transitions from B2 to B1 and vice versa have staggering with an opposite phase. This behavior is different from the one seen in Ref. [12] due to the smaller value of  $\gamma$  and significant mixing of several single-particle levels.

In the case of  $^{130}\text{Cs}$ , the  $B(E2)$  values are similar for both bands and in a nice agreement with the measured ones except for an abrupt behavior at  $I = 14\hbar$  due to the reason explained above. Similarly, the  $B(M1)$  values and  $B(M1)/B(E2)$  ratios also agree with the experimental data and show staggering as expected in chiral bands [24]. The interband  $B(M1)$  values for the transitions from band B2 to B1 agree well in magnitude with the experimental data but the phase of staggering is opposite. The interband  $B(M1)$  values for the transitions from band B1 to B2 show staggering opposite to the intraband trends supporting chirality [24], while staggering is not present for transitions from band B2 to B1.

In case of  $^{130}\text{La}$ , similar to  $^{128}\text{Cs}$ , the  $B(E2)$  values are comparable for both bands and agree well with the experimental data except at higher spins. The  $B(M1)$  and  $B(M1)/B(E2)$  values for band B1 show staggering, while there is no staggering in the case of band B2. The calculated interband  $B(M1)$  values for transitions from band B2 to B1 and vice versa are similar in magnitude, but the staggering is enhanced in B1 to B2 transitions at higher spins. The  $B(M1)$  values for transitions from B2 to B1 are comparable with the measured ones. Our results show better agreement with the experimental data than the results of two-quasiparticles-plus-rotor model (TQRM) reported in Ref. [8].

With the nice agreement of calculated rotational energies and EM transition probabilities with the experimental data, we proceed to investigate the other properties of doublet bands which cannot be measured directly but can provide the details on the possible chiral symmetry breaking. Some of these properties are the orientation of total angular momentum  $I$  on the tilted  $(\theta, \phi)$  plane, i.e., the angular momentum profile  $\mathcal{P}^I(\theta, \phi)$  [Eq. (6)], the single-particle configurations of both bands, and the projection of individual angular momentum of proton, neutron, and the core on all three principal axes.

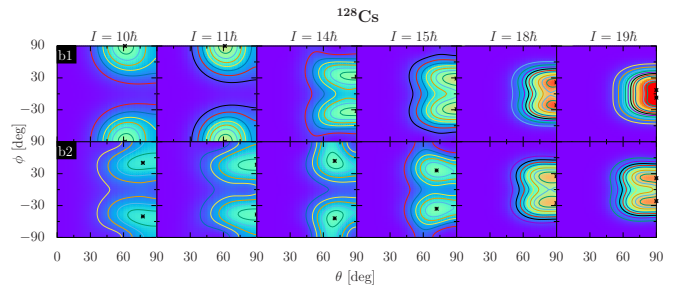
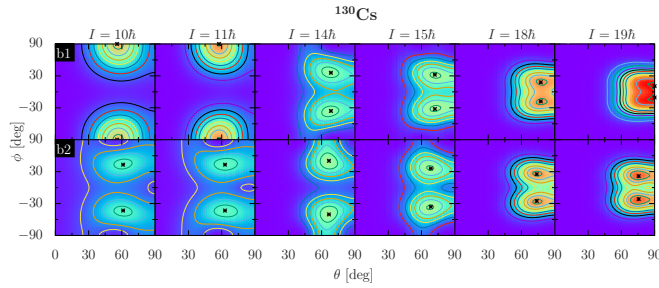


FIG. 3. Azimuthal plots for the doublet bands B1 (upper panels) and B2 (lower panels) in  $^{128}\text{Cs}$  for selected spins.

The profile  $\mathcal{P}^I(\theta, \phi)$ , also called azimuthal plots [12,14,17], for doublet bands in  $^{128}\text{Cs}$  for selected interesting cases is shown in Fig. 3. At  $I = 10\hbar$  and  $11\hbar$ , the peaks of  $\mathcal{P}^I(\theta, \phi)$  for B1 are situated at  $[\theta, \phi]$  of the order of  $\{\approx 60^\circ, \approx -90^\circ \text{ and } 90^\circ\}$  ( $sl$  plane). This is consistent with a recent experimental study [10] which provided a direct evidence for the planar motion at the band head ( $9\hbar$ ) of the yrast band through the measurement of its  $g$  factor. In the case of B2, the peaks are present at  $\{\approx 75^\circ, \approx -50^\circ \text{ and } 50^\circ\}$  (aplanar) and  $\{\approx 90^\circ, \approx -50^\circ \text{ and } 50^\circ\}$  ( $si$  plane) for  $10\hbar$  and  $11\hbar$ , respectively. These peaks are not distinct due to the significant spread of profiles over a broad range of  $\theta$ . Hence, the weak chiral vibrations can be expected at these lower spins. For  $I = 14\hbar$ , the peaks are located distinctly at  $\{\approx 90^\circ, \approx -30^\circ \text{ and } 30^\circ\}$  ( $si$  plane) and  $\{\approx 70^\circ, \approx -45^\circ \text{ and } 45^\circ\}$  (aplanar) in the case of bands B1 and B2, respectively. A similar behavior is present at  $I = 15\hbar$  favoring chiral vibrations [12,15] in this spin region. At  $I = 14\hbar$  in B1, the study based on AMP [12] suggested an aplanar orientation of the angular momentum. This contradiction with our results is due to the assumption in AMP that the valence proton and neutron are considered as occupying the first and fourth orbitals of  $h_{11/2}$ , respectively, whereas we considered the mixing of other single-particle levels which can change the orientation significantly. At  $I = 18\hbar$ , in the case of both bands, the peaks are present at  $\{\approx 90^\circ, \approx -20^\circ \text{ and } 20^\circ\}$  ( $si$  plane), signifying the tendency of  $I$  to align along the  $i$  axis. Hence, chirality is weakened in this spin region. At  $I = 19\hbar$ , the angular momentum lies along the  $i$  axis and in the  $si$  plane with angles  $\{\approx 90^\circ, \approx 0^\circ\}$  and  $\{\approx 90^\circ, \approx -20^\circ \text{ and } 20^\circ\}$  in the case of bands B1 and B2, respectively. These orientations do not support chirality, and hence imply that in  $^{128}\text{Cs}$ , the onset of chirality disappearance happens at  $I = 19\hbar$ . It can be noticed that in contrast to other studies [7,12], static chirality is not supported by our calculations.

The azimuthal plots for  $^{130}\text{Cs}$  are given in Fig. 4. At  $I = 10\hbar$  and  $11\hbar$ , the peaks of  $\mathcal{P}^I(\theta, \phi)$  in the case of bands B1 and B2 are distinctly located at  $[\theta, \phi]$  of the order of  $\{\approx 60^\circ, \approx -90^\circ \text{ and } 90^\circ\}$  ( $sl$  plane) and  $\{\approx 60^\circ, \approx -45^\circ \text{ and } 45^\circ\}$  (aplanar), respectively. These orientations clearly indicate the appearance of chiral vibrations. At  $I = 14\hbar$ , the peaks are present at  $\{\approx 65^\circ, \approx -45^\circ \text{ and } 45^\circ\}$  (aplanar) for both bands. A similar behavior is present at  $I = 15\hbar$ . Hence, static chirality is realized in this spin region. At  $I = 18\hbar$ ,



FIG. 4. Same as in Fig. 3 but for  $^{130}\text{Cs}$ .

the total angular momentum approaches the  $i$  axis, leading the peaks to be at  $\{\approx 75^\circ, \approx -15^\circ$  and  $15^\circ\}$  (aplanar) and  $\{\approx 75^\circ, \approx -30^\circ$  and  $30^\circ\}$  (aplanar) for bands B1 and B2, respectively. From these orientations we infer that chirality weakens at  $18\hbar$ . At  $I = 19\hbar$ , where the peaks are located at  $\{\approx 90^\circ, \approx 0^\circ\}$  ( $i$  axis) and  $\{\approx 75^\circ, \approx -20^\circ$  and  $20^\circ\}$  (aplanar) for bands B1 and B2, respectively, we observe that chirality almost disappears. Our results are very similar to the ones obtained with the projected shell model [14], where a proper mixing of the single-particle levels is considered.

The azimuthal plots for  $^{130}\text{La}$  are given in Fig. 5. At  $I = 10\hbar$  and  $11\hbar$ , the peaks for the profile  $\mathcal{P}^I(\theta, \phi)$  are present at  $[\theta, \phi]$  of the order of  $\{\approx 60^\circ, \approx -90^\circ$  and  $90^\circ\}$  ( $sl$  plane) and  $\{\approx 60^\circ, \approx -45^\circ$  and  $45^\circ\}$  (aplanar) for bands B1 and B2, respectively. However, the distribution is significant for a broad range of  $\theta$ . These observations suggest weak chiral vibrations at lower spins. At  $I = 14\hbar$ , in the case of bands B1 and B2, the peaks appear at  $\{\approx 80^\circ, \approx -30^\circ$  and  $30^\circ\}$  (aplanar) and  $\{\approx 65^\circ, \approx -45^\circ$  and  $45^\circ\}$  (aplanar), respectively. In the case of band B1, the peaks are not distinct and a large value of  $\theta$  indicates the tendency of inclination in the  $si$  plane. Hence, static chirality can be expected, but with a lower probability. At  $I = 15\hbar$ , the peaks are obtained at  $\{\approx 90^\circ, \approx 0^\circ\}$  ( $i$  axis) and  $\{\approx 70^\circ, \approx -45^\circ$  and  $45^\circ\}$  (aplanar) in the case of bands B1 and B2, respectively. These orientations suggest a weak chiral vibration mode. At  $I = 18\hbar$  and  $19\hbar$ , the peaks are located at  $\{\approx 90^\circ, \approx 0^\circ\}$  ( $i$  axis) and  $\{\approx 90^\circ, \approx -25^\circ$  and  $25^\circ\}$  ( $si$  plane) for bands B1 and B2, respectively. These orientations do not support chirality, and indicate disappearance of chirality at high spins due to the inclination of  $I$  towards the  $i$  axis. Furthermore, the possibility of achieving static chirality at  $I = 14\hbar$  spin is larger in  $^{130}\text{La}$  than in  $^{128}\text{Cs}$ . Our investigations of chiral geometry through  $K$  plots lead to similar conclusions, and are not shown here.

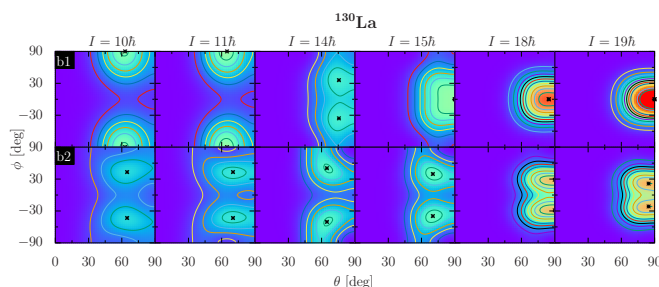
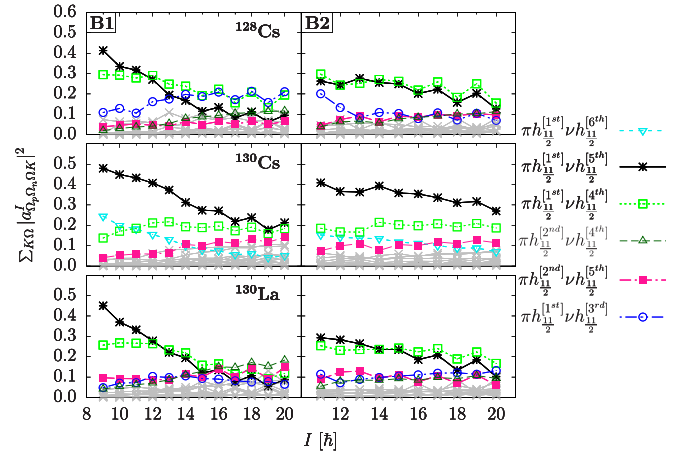
FIG. 5. Same as in Fig. 3 but for  $^{130}\text{La}$ .

FIG. 6. Contributions of single-particle configurations as a function of spin ( $I$ ) for bands B1 (left panels) and B2 (right panels) in  $^{128}\text{Cs}$  (top),  $^{130}\text{Cs}$  (middle), and  $^{130}\text{La}$  (bottom). The configurations having dominant contributions are represented by colored lines and labeled. The grey lines represent the configurations with negligible contributions.

For a prominent chiral geometry, we require three mutually perpendicular angular momenta. The best way to achieve this is to have one valence nucleon occupying a lower and the other occupying an upper orbital of a high  $j$  shell. In the case of  $^{130}\text{Cs}$ , the contributions of single-particle configurations shown in Fig. 6 reveal that for both bands  $\{\pi h_{11/2}^{[1st]} \otimes \nu h_{11/2}^{[5th]}\}$  is the dominant configuration at the band head. At higher spins, other configurations like  $\{\pi h_{11/2}^{[1st]} \otimes \nu h_{11/2}^{[4th]}\}$  also contribute significantly. Our results show a notable contribution of the  $\nu h_{11/2}^{[6th]}$  orbital, which was not considered in the calculations based on the projected shell model [14]. However, we do not see an observable impact of this orbital in our final results. Since the proton and neutron are lying in the lower and upper orbitals of the  $h_{11/2}$ , they orient along the short ( $s$ ) and long ( $l$ ) axis, respectively. The dominant configuration is the same for the bands in a broad spin region, and hence support the achievement of static chirality. At  $I = 14\hbar$ , the trend of increase or decrease in the contribution of several configurations changes in both bands. For example, an almost linear increment (decrement) in the contribution of the configuration  $\{\pi h_{11/2}^{[1st]} \otimes \nu h_{11/2}^{[4th]}\}$  with spin suddenly decreases (increases) at  $I = 14\hbar$  in B1 (B2). These changes further explain the abrupt behavior observed in EM transition probabilities (see Fig. 2).

In the case of  $^{128}\text{Cs}$ , the configurations  $\{\pi h_{11/2}^{[1st]} \otimes \nu h_{11/2}^{[5th]}\}$  and  $\{\pi h_{11/2}^{[1st]} \otimes \nu h_{11/2}^{[4th]}\}$  have dominant contribution at band heads. Above  $I = 13\hbar$ , in case of band B1,  $\{\pi h_{11/2}^{[1st]} \otimes \nu h_{11/2}^{[3rd]}\}$  becomes the dominating configuration instead of  $\{\pi h_{11/2}^{[1st]} \otimes \nu h_{11/2}^{[5th]}\}$ . Therefore, we observe an abrupt behavior in EM transition probabilities at  $I = 14\hbar$  (see Fig. 2). The probability of the neutron level aligning along the  $l$  axis is reduced due to the dominance of  $\nu h_{11/2}^{[3rd]}$ . Subsequently (unlike B2) the aplanar motion is not achieved and therefore static chirality is hindered.

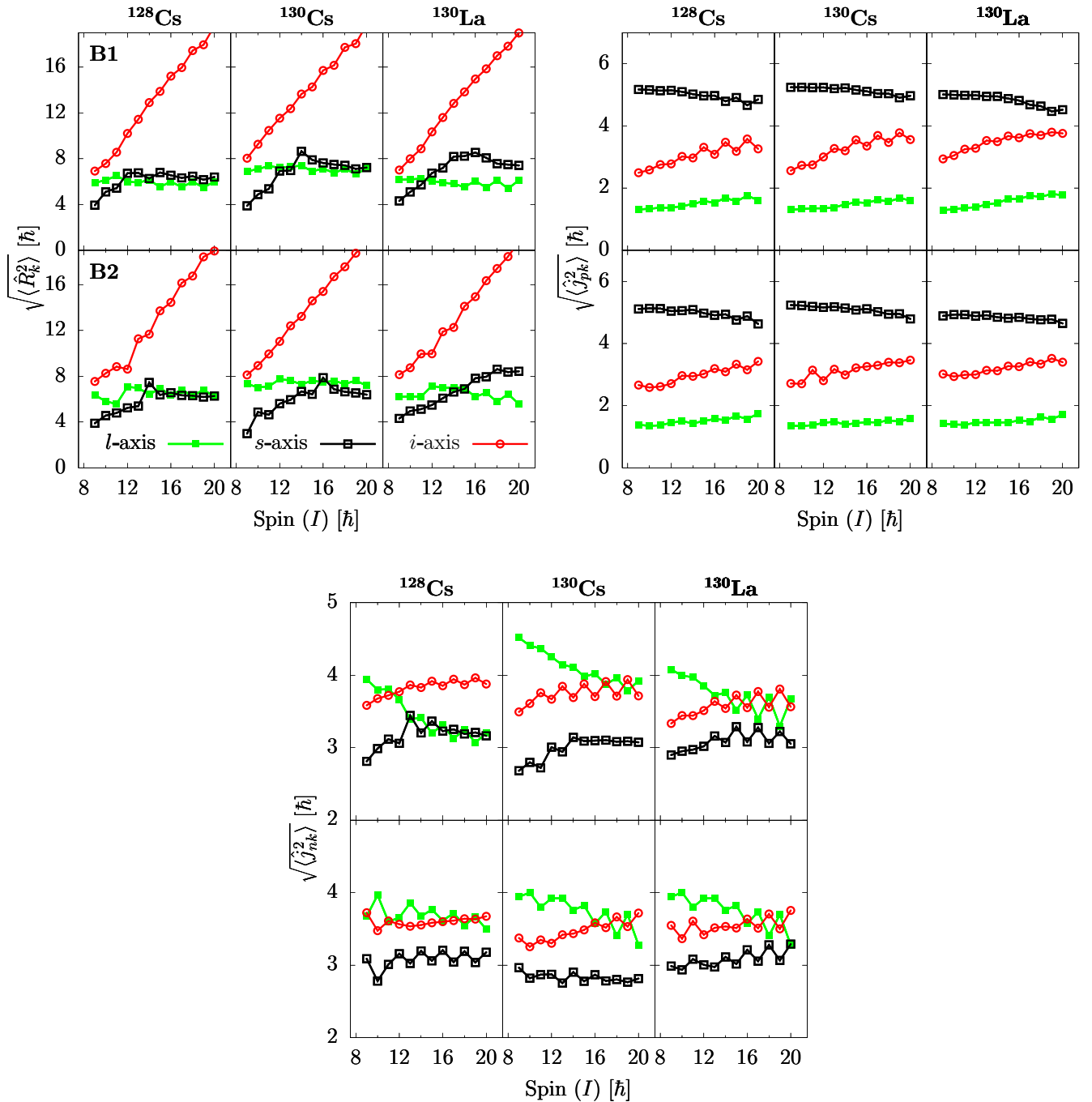


FIG. 7. Root mean square (rms) values of the core ( $R$ ), proton ( $j_p$ ), and neutron ( $j_n$ ) angular momentum components along the intermediate ( $i$ ), short ( $s$ ), and long ( $l$ ) axes denoted by  $k$  for the bands B1 and B2 in  $^{128}\text{Cs}$ ,  $^{130}\text{Cs}$ , and  $^{130}\text{La}$ .

In the case of  $^{130}\text{La}$ , at the band head,  $\{\pi h_{11/2}^{[1st]} \otimes \nu h_{11/2}^{[5th]}\}$  and  $\{\pi h_{11/2}^{[1st]} \otimes \nu h_{11/2}^{[4th]}\}$  are dominant configurations for both bands. We observe an indication of static chirality at  $I = 14\hbar$  due to the critical angular momentum required to achieve it [26], and similar configuration for both bands. However, this indication is weaker (compared to  $^{130}\text{Cs}$ ) due to a strong mixing of other levels. In band B1, beyond spin  $15\hbar$ , many configurations, which do not support chirality, have a strong mixing.

For all the considered nuclei, we observe that at higher spins the contributions of single-particle configurations have an odd-even staggering with opposite phases for bands B1 and B2. This staggering is in phase with that of the rotational energies [see  $S(I)$  in Fig. 1]. This allows us to establish that the staggering in rotational energies is due to the variation in the contribution of single-particle configurations.

The root mean square (rms) values of the angular momentum components of proton, neutron, and core along three principal axes ( $l$ ,  $s$ ,  $i$ ) are given in Fig. 7. At the band heads in

both the bands, the rms value of the components of the core angular momentum  $R$  along all three axes is significant with its maximum along the  $i$  axis. Increasing the total angular momentum  $I$ , the rms value of the component along the  $i$  axis increases sharply due to the maximum moment of inertia along this axis. At higher spins, in the case of  $^{128,130}\text{Cs}$ , the rms values of the components along the  $s$  and  $l$  axes are almost equal due to  $\gamma = 28^\circ$  (closer to maximal triaxiality,  $\gamma = 30^\circ$ ), whereas in the case of  $^{130}\text{La}$ , the value along the  $s$  axis is larger than that along the  $l$  axis due to the smaller value of  $\gamma = 23^\circ$ . The rms value of the proton angular momentum  $j_p$  is maximum for its component along the  $s$  axis. Since the valence proton is occupying the lower orbitals of  $h_{11/2}$  (where there are no orbitals from other shells), the effect of Coriolis interaction gets weaker with the increase in spin.

The rms values of the components of neutron angular momentum  $j_n$  along all three principal axes are significant. The Fermi level of the neutron corresponds to a higher orbital of  $h_{11/2}$  which is closer to the orbitals of the next shell. This favors the Coriolis interaction which strongly affects the orientation of  $j_n$ . At the band head of B1 in  $^{128}\text{Cs}$ , the rms value of  $j_n$  is maximum along the  $l$  axis, while with an increase in spin, it becomes maximum along the  $i$  axis. In the case of B2, the rms values of the  $j_n$  components along the  $l$  and  $i$  axes are almost equal throughout the considered spin region. For  $^{130}\text{Cs}$  and  $^{130}\text{La}$ , the trend of rms values of  $j_n$  is the same for both bands. At lower spins, these values are maximum along the  $l$  axis. With an increase in spin, the rms value of the  $j_n$  component along the  $i$  axis increases and becomes almost equal to that along the  $l$  axis at higher spins. It happens sooner in  $^{130}\text{La}$  (at  $I = 13\hbar$  in B1) than in  $^{130}\text{Cs}$  (at  $I = 15\hbar$ ). Also, in the case of  $^{130}\text{La}$ , the rms value of the  $j_n$  component along the  $s$  axis is comparable to those along the  $l$  and  $i$  axes.

One can notice that the core and proton orientations are in favor of static chirality in all three nuclei. Therefore, the neutron orientation turns out to be the decisive factor to set up the mode of chirality, i.e., static or vibrational. Furthermore, the odd-even staggering in the rms values of  $j_p$  and  $j_n$  com-

ponents originate from the differences in the single-particle configurations (see Fig. 6).

The arguments from the analyses of all quantities are in support of each other without causing any ambiguity. Comparing all cases for different quantities from rotational energies to azimuthal plots and single-particle configurations, the  $^{130}\text{Cs}$  qualifies as the best example of chirality in contrast to  $^{128}\text{Cs}$  as suggested in many other studies [7,12]. This fact can be attributed to the nature of single-particle configurations as they remain similar for both bands in  $^{130}\text{Cs}$  throughout the probable chirality region.

#### IV. CONCLUSIONS

Chiral doublet bands in  $^{128}\text{Cs}$ ,  $^{130}\text{Cs}$ , and  $^{130}\text{La}$  are studied within the nonadiabatic quasiparticle approach. The theoretical study of  $^{130}\text{La}$  through chiral geometry and its correlation with single-particle configurations are presented for the first time. The chiral vibration mode is found to be dominant, but a weak indication of static chirality is also present at  $I = 14\hbar$ .

The energy spectra and the reduced electromagnetic transition probabilities agree well with the experimental data for all three nuclei. Chiral geometry is investigated through the azimuthal plots. The dependence of the chirality mode on the single-particle configurations is demonstrated. The rms values of the angular momentum components of proton, neutron, and core along three principal axes suggest that the chirality mode depends on the neutron orientation in the nuclei considered.

Our results do not support static chirality in  $^{128}\text{Cs}$  in contrast to earlier studies [7,12]. There are clear indications of static chirality in  $^{130}\text{Cs}$  for a significant range of spin. Based on the comparison of all calculated properties,  $^{130}\text{Cs}$  qualifies as a better example for chirality than  $^{128}\text{Cs}$ . It would be interesting to see the validity of our arguments by measuring  $g$  factors for higher levels of chiral bands. Such measurements will further improve our understanding of the role of single-particle configuration mixing emphasizing the importance of a nonadiabatic treatment.

- 
- [1] S. Frauendorf and J. Meng, *Nucl. Phys. A* **617**, 131 (1997).  
 [2] B. Xiong and Y. Wang, *At. Data Nucl. Data Tables* **125**, 193 (2019).  
 [3] J. Meng and S. Q. Zhang, *J. Phys. G: Nucl. Part. Phys.* **37**, 064025 (2010).  
 [4] J. Meng, Q. B. Chen, and S. Q. Zhang, *Int. J. Mod. Phys. E* **23**, 1430016 (2014).  
 [5] J. Meng and P. Zhao, *Phys. Scr.* **91**, 053008 (2016).  
 [6] A. A. Raduta, *Prog. Part. Nucl. Phys.* **90**, 241 (2016).  
 [7] E. Grodner, J. Srebrny, A. A. Pasternak, I. Zalewska, T. Morek, Ch. Droste, J. Mierzejewski, M. Kowalczyk, J. Kownacki, M. Kisieliński, S. G. Rohoziński, T. Koike, K. Starosta, A. Kordyasz, P. J. Napiorkowski, M. Wolińska-Cichocka, E. Ruchowska, W. Plóciennik, and J. Perkowski, *Phys. Rev. Lett.* **97**, 172501 (2006).  
 [8] M. Ionescu-Bujor, S. Aydin, N. Mărginean, C. Costache, D. Bucurescu, N. Florea, T. Glodariu, A. Ionescu, A. Iordăchescu, R. Mărginean, C. Mihai, R. E. Mihai, A. Mitu, A. Negreț, C. R. Niță, A. Olăcel, S. Pascu, B. Saygi, L. Stroe, R. Suvăilă, S. Toma, and A. Turturică, *Phys. Rev. C* **98**, 054305 (2018).  
 [9] D. Tonev, G. de Angelis, P. Petkov, A. Dewald, S. Brant, S. Frauendorf, D. L. Balabanski, P. Pejovic, D. Bazzacco, P. Bednarczyk *et al.*, *Phys. Rev. Lett.* **96**, 052501 (2006).  
 [10] E. Grodner, J. Srebrny, Ch. Droste, L. Próchniak, S. G. Rohoziński, M. Kowalczyk, M. Ionescu-Bujor, C. A. Ur, K. Starosta, T. Ahn, M. Kisieliński, T. Marchlewski, S. Aydin, F. Recchia, G. Georgiev, R. Lozeva, E. Fiori, M. Zielińska, Q. B. Chen, S. Q. Zhang, L. F. Yu, P. W. Zhao, and J. Meng, *Phys. Rev. Lett.* **120**, 022502 (2018).  
 [11] B. Qi, S. Q. Zhang, J. Meng, S. Y. Wang, and S. Frauendorf, *Phys. Lett. B* **675**, 175 (2009).  
 [12] F. Q. Chen, Q. B. Chen, Y. A. Luo, J. Meng, and S. Q. Zhang, *Phys. Rev. C* **96**, 051303(R) (2017).  
 [13] Q. B. Chen and J. Meng, *Phys. Rev. C* **98**, 031303(R) (2018).

- [14] F. Q. Chen, J. Meng, and S. Q. Zhang, *Phys. Lett. B* **785**, 211 (2018).
- [15] J. Peng and Q. B. Chen, *Phys. Lett. B* **793**, 303 (2019).
- [16] P. Siwach, P. Arumugam, S. Modi, L. S. Ferreira, and E. Maglione, *J. Phys. G: Nucl. Part. Phys.* **47**, 125105 (2020).
- [17] P. Siwach, P. Arumugam, L. S. Ferreira, and E. Maglione, *Phys. Lett. B* **811**, 135937 (2020).
- [18] P. Arumugam, E. Maglione, and L. S. Ferreira, *Phys. Rev. C* **76**, 044311 (2007).
- [19] A. J. Simons, P. Joshi, D. G. Jenkins, P. M. Raddon, R. Wadsworth, D. B. Fossan, T. Koike, C. Vaman, K. Starosta, E. S. Paul *et al.*, *J. Phys. G: Nucl. Part. Phys.* **31**, 541 (2005).
- [20] T. Koike, K. Starosta, C. J. Chiara, D. B. Fossan, and D. R. LaFosse, *Phys. Rev. C* **63**, 061304(R) (2001).
- [21] M. Ionescu-Bujor, A. Iordăchescu, N. Mărginean, R. Lica, D. Bucurescu, F. Brandolini, D. Deleanu, D. Filipescu, I. Gheorghe, D. Ghiță, T. Glodariu, R. Mărginean, N. H. Medina, C. Mihai, A. Negret, L. Stroe, and C. A. Ur, *Phys. Rev. C* **90**, 014323 (2014).
- [22] P. Möller, A. Sierk, T. Ichikawa, and H. Sagawa, *At. Data Nucl. Data Tables* **109-110**, 1 (2016).
- [23] S. Modi, M. Patial, P. Arumugam, E. Maglione, and L. S. Ferreira, *Phys. Rev. C* **95**, 024326 (2017).
- [24] T. Koike, K. Starosta, and I. Hamamoto, *Phys. Rev. Lett.* **93**, 172502 (2004).
- [25] P. Ring and P. Schuck, *The Nuclear Many-Body Problem* (Springer-Verlag, Berlin, 1980).
- [26] P. Olbratowski, J. Dobaczewski, J. Dudek, and W. Płóciennik, *Phys. Rev. Lett.* **93**, 052501 (2004).